Nano-Micro Letters

e-ISSN 2150-5551
CN 31-2103/TB

ARTICLE

https://doi.org/10.1007/s40820-026-02195-8

Cite as
Nano-Micro Lett.
(2026) 18:349

Received: 24 December 2025
Accepted: 1 April 2026

Dual-Functional Photonic Metacoating Integrating Fluorescence Thermometry and High-Performance Space Radiative Cooling

Hao Gong[1], Zhongyang Wang[1] ✉, Yan Zheng[1], Liping Tong[2], Hongchao Li[1], Zhiyuan Zhao[1], Junjia Liu[1], Gang Liu[3], Xiao Zhou[1] ✉, Tongxiang Fan[1] ✉

HIGHLIGHTS

- Dual-functional Eu-doped ZrO_2 submicrosphere metacoating for space radiative cooling and fluorescence thermometry.
- Photonic structure and materials co-design yield an ultralow solar absorptance ($\alpha_s = 0.076$) and high emittance ($\varepsilon = 0.931$) in a ~ 100 μm thick metacoating.
- The metacoating achieves a net cooling power of 323.69 W m^{-2} and enables 173–433 K non-contact thermometry ($S_{r,max} = 0.797\%\ K^{-1}$) with reliable irradiation resistance under space environments.

ABSTRACT Fluorescence thermometry offers a non-contact strategy for early detection of thermal instabilities on complex spacecraft surfaces, enabling reliable in-orbit temperature mapping. However, simultaneously achieving high-sensitivity fluorescence thermometry and efficient space radiative cooling remains challenging, as enhanced visible absorption improves thermometric response but increases solar heating. Here, we address this trade-off through a material-structure co-design strategy by developing an Eu-doped ZrO_2 submicrosphere metacoating that integrates space radiative cooling with fluorescence-based temperature sensing. Guided by photonic-structure optimization using a constrained-gradient optimizer combined with grid-search mapping, the optimized metacoating, featuring a submicrosphere diameter of 0.756 μm and a volume fraction of 35%, achieves an ultralow solar absorptance ($\alpha_s = 0.076$) and a high thermal emittance ($\varepsilon = 0.931$). In parallel, bandgap-driven compositional optimization identifies an optimal Eu content of 8.48%, enabling outstanding thermometric performance. The metacoating delivers a net cooling power of 323.69 W m^{-2} and a 77 °C temperature reduction relative to an Al sheet, outperforming representative oxide-based inorganic coatings. It allows temperature sensing over 173–433 K with a maximum relative sensitivity of 0.797% K^{-1}, surpassing fluorescent oxides with comparable absorption edges. Moreover, the metacoating maintains the lowest α_s and reliable irradiation resistance under proton, electron, atomic oxygen and ultraviolet exposures, outperforming reported counterparts. Together with its scalable fabrication, this work establishes a dual-functional metacoating platform for intelligent spacecraft thermal management that combines efficient radiative cooling with high-sensitivity fluorescence thermometry.

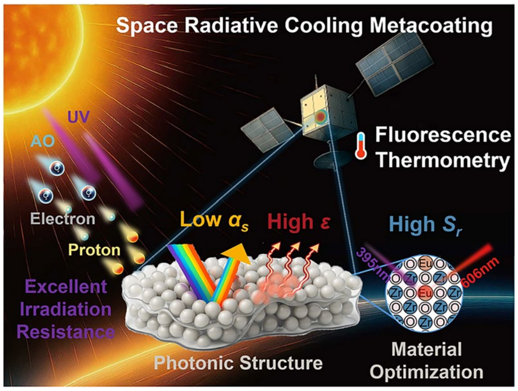

KEYWORDS Photonic metacoating; Eu-doped ZrO_2 submicrosphere; Space radiative cooling; Fluorescence thermometry

---

✉ Zhongyang Wang, zy_wang@sjtu.edu.cn; Xiao Zhou, zhouxiao113@sjtu.edu.cn; Tongxiang Fan, txfan@sjtu.edu.cn
[1] State Key Laboratory of Metal Matrix Composites, School of Materials Science and Engineering, Shanghai Jiao Tong University, Shanghai 200240, People's Republic of China
[2] School of Materials, Shanghai Dianji University, Shanghai 201306, People's Republic of China
[3] Shanghai Institute of Spacecraft Equipment, Shanghai 200240, People's Republic of China

1 Introduction

Thermal management defines the operational limits of spacecraft, as temperature fluctuations can directly compromise the performance of high-power missions [1]. Traditional radiative cooling coatings combining low solar absorptance (α_s), high thermal emittance (ε) and thin-film design offer a transformative, zero-energy route to passive thermal regulation by efficiently dissipating heat to the deep-space cold sink [2–5]. To suppress solar input, high refractive index or wide bandgap (E_g) oxides such as ZnO [6], Zn_2SiO_4 [7], $MgGa_2O_4$ [8] and ZrO_2 [9], are typically employed to maximize solar backscattering. However, conventional oxide coatings lack in situ health monitoring capability, making the integration of precise and rapid temperature sensing essential for early detection of thermal anomalies and for maintaining spacecraft reliability. Traditional thermometric approaches (such as thermocouples, infrared thermography and thermosensitive paints) are hindered by wiring complexity, thermal perturbation or limited accuracy, rendering them unsuitable for extreme space environments [10, 11]. In contrast, fluorescence thermometry offers a non-contact and high-spatial-resolution optical solution that is independent of surface emissivity and resistant to electromagnetic interference, suiting the harsh space environment [12, 13]. Integrating such fluorescent thermometry into radiative cooling coatings thus represents a significant step toward intelligent thermal management systems that combine efficient passive cooling with real-time, self-perceptive temperature sensing.

Building on the concept of integrating fluorescence thermometry into radiative cooling coatings, the material must meet stringent requirements, combining a luminescent center that delivers strong and temperature-sensitive emissions with a host matrix that exhibits minimal α_s to maintain efficient radiative cooling performance. Rare-earth ions are ideal emitters because their 4*f* orbitals are shielded by outer 5*s* and 5*p* electrons, which suppresses environmental perturbations and yields sharp, well-defined emission lines [14, 15]. Parity-allowed 4*f*-5*d* transitions offer efficient excitation but introduce broadband visible absorption that can elevate α_s, whereas parity-forbidden 4*f*-4*f* transitions are largely host-insensitive and arise from highly localized 4*f* states. These discrete intra-4*f* levels enable radiative processes without materially altering the host E_g. Recent strategies have often employed narrow E_g host materials such as $ZrTiO_4$ [16], $Sr_2NaMg_2V_3O_{12}$ [17], Ba_2LuNbO_6 [18] and $LiY_6(BO_3)_3O_5$ [19] to enhance thermometric sensitivity by strengthening the coupling between host absorption and rare-earth excitation or emission processes. However, this approach unavoidably increases visible absorption and degrades radiative cooling performance. A viable path is therefore to pair luminescent rare-earth ions with a wide E_g host that preserves low α_s while maintaining robust, temperature-responsive luminescence.

Overcoming the above trade-off between high-sensitivity fluorescence thermometry and minimal α_s remains a major challenge. To address this, Eu^{3+} ions offer a particularly promising route, as their excitation bands lie in the UV region and their large Stokes shift prevents self-absorption within the solar spectrum, thereby avoiding parasitic heating. The hypersensitive $^5D_0 \rightarrow {}^7F_2$ transition in the red region shows narrow linewidths and strong temperature dependence, enabling reliable fluorescence-intensity-ratio (FIR) based thermometry [20, 21]. ZrO_2 serves as an ideal host with a wide E_g and low phonon energy, which suppresses nonradiative losses and enhances emission efficiency [22, 23]. In addition, its high refractive index, combined with optimized submicrosphere-based random scattering photonic structure, facilitates maximized solar backscattering, thereby achieving ultralow α_s [24–27].

Here, we present a dual-functional photonic metacoating that integrates high-sensitivity fluorescence thermometry with high-performance space radiative cooling, enabling real-time optical temperature readout while passively maintaining low surface temperatures under solar loading and stability under space irradiation environment, including proton, electron, atomic oxygen (AO), ultraviolet (UV), as well as thermal cycling (Fig. 1a, b). Guided by photonic structure design using a constrained gradient optimizer combined with grid search mapping, together with E_g engineering driven compositional optimization enabled by the controlled synthesis of Eu-doped ZrO_2 submicrospheres (EZS), we identify an optimal Eu content of 8.48% and a photonic configuration with a submicrosphere diameter of 0.756 μm at a volume fraction of 35%. The resulting EZS metacoating delivers an ultralow α_s of 0.076 together with a high ε of 0.931, enabling a maximum net cooling power of 323.69 W m^{-2} and outperforming state-of-the-art counterparts. Under simulated vacuum space conditions, it reduces the temperature of an

Al sheet by approximately 77 °C and achieves a significantly lower steady state temperature than conventional oxide coatings. Thermometrically, the metacoating attains a peak relative sensitivity S_r of 0.797% K^{-1} and exceeds systems with comparable or even shorter absorption edges ($\lambda_g = 1240/E_g$), highlighting its superior thermometric sensitivity. The metacoating maintains consistently lowest α_s before and after proton, electron, AO, UV and combined irradiations, in contrast to the degradation observed in commercial and literature-reported coatings, underscoring its irradiation durability. Consequently, this work delivers the strong potential of an integrated, non-contact optical-thermometry and space radiative cooling metacoating for long-term, stable thermal management of spacecraft.

2 Experimental Section

2.1 Synthesis of EZS and Fabrication of Metacoating

EZS were prepared by modifying previously reported route for undoped ZrO_2 submicrospheres (ZS) [28]. Typically, 0.4 mmol stearic acid, 20 mmol triethanolamine and a defined amount of water were dissolved in 200 mL of ethanol and stirred for 1 h. Zirconium propoxide solution (15 mmol) was then rapidly injected, and the mixture was left to react for a total of 150 min under gentle stirring. The resulting ZS precursor was collected by centrifugation and redispersed in 20 mL of ethanol. The particle size was tuned either by varying the water content (54, 40.5, or 27 mmol) or by replacing 25 mL of ethanol with methanol while keeping the water content at 36 mmol.

For Eu incorporation, the ZS precursor was transferred into 100 mL aqueous Eu^{3+} solutions (0.0002, 0.002, 0.02 or 0.2 mol L^{-1}) in a 200 mL Teflon-lined autoclave and treated hydrothermally at 180 °C for 24 h. The resulting EZS precursors were separated by centrifugation, washed, dried at 120 °C for 4 h, and then calcined at 600, 800, 1000 or 1200 °C to induce crystallization. The final EZS exhibited mean diameters of 0.254, 0.525, 0.756 and 1.049 µm, respectively.

Metacoatings with EZS volume fractions of 15%, 25%, 35% and 45% were produced by spray coating. A diluted aqueous K_2SiO_3 binder solution was mixed with EZS and ball-milled at 120 rpm for 180 min to obtain a homogeneous slurry, which was then sprayed onto pre-sanded Al substrates. After drying at ambient conditions for 48 h, uniform metacoatings with various thicknesses were obtained. As a direct comparison to our previously reported coating [29], ZnO, TiO_2 and Zn_2TiO_4 coatings were fabricated using the same K_2SiO_3 matrix and spray-coating protocol, with a fixed pigment volume fraction of 35% and a comparable thickness of ~ 100 µm.

2.2 Optical Performance Characterizations

The optical E_g and reflectance were measured using a UV–Vis-NIR spectrophotometer (PerkinElmer Lambda 950, USA) equipped with a 15 cm integrating sphere. Spectra were collected from 0.25 to 2.5 µm, using polytetrafluoroethylene as the reflectance standard. Thermal emittance in the 2.5–25 µm range was obtained with a Fourier transform infrared spectrometer (FTIR, Bruker INVENIO-R, Germany) coupled to a gold-coated integrating sphere (Bruker A562). Fluorescence properties were characterized by using a fluorescence spectrometer (FLS920, Edinburgh Instruments, UK). Excitation and emission spectra were further measured on a spectrofluorometer (Horiba Jobin Yvon Fluorolog-3, HORIBA Jobin Yvon, France) equipped with a 450 W Xenon lamp. The same system, fitted with an integrating sphere, was used to determine fluorescence lifetime decay.

2.3 Field Tests

Radiative cooling performance was evaluated in a vacuum blackbody chamber maintained below 10^{-3} Pa. Samples were illuminated with an AM0 solar simulator (SSS-500-A, Nmerry Technology Co., Ltd., China). A polyimide heater (~ 2 W) attached to the rear of the coated Al substrate mimicked internal heat generation. Temperatures were monitored in real time using a CENTER 309 thermometer (Qunte Technology Co., Ltd., Taiwan), with the thermocouple routed through a vacuum feedthrough to ensure accurate measurements.

Irradiation resistance was examined at the Shanghai Institute of Spacecraft Equipment using dedicated radiation facilities. Tests were conducted at 298 ± 5 K and ~ 10^{-5} Pa. Proton irradiation was performed at 50 keV with a fluence of 1.0×10^{12} p cm^{-2}, while electron irradiation used 50 keV

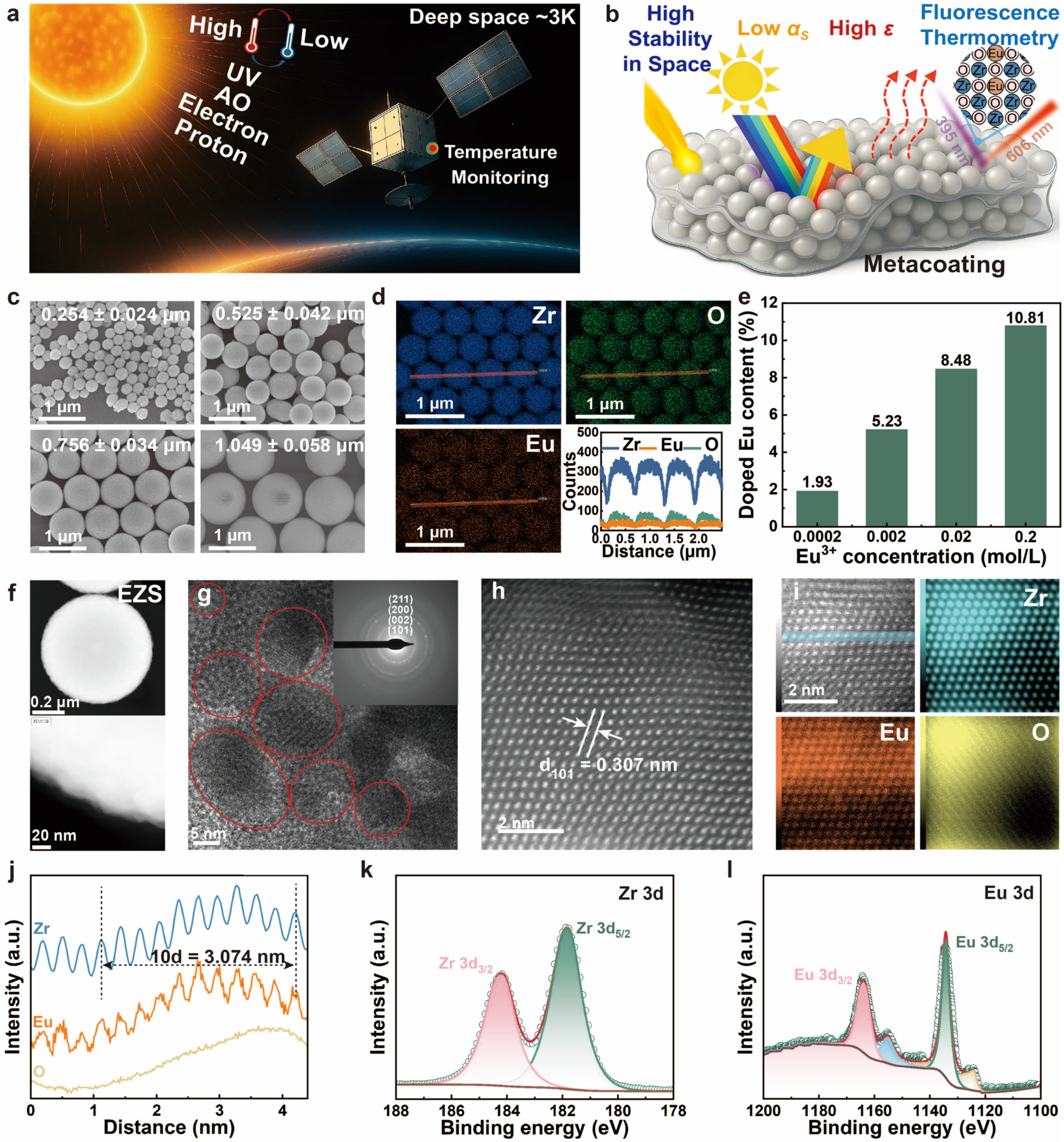

Fig. 1 Working mechanism of the EZS metacoating and the characterization of EZS. **a** Schematic of proton, electron, AO and UV exposures, thermal cycling, and temperature monitoring on spacecraft surfaces. **b** Concept of the EZS metacoating integrating low α_s, high ε, fluorescence thermometry and excellent durability under space environments. **c** SEM images of EZS with diameters of 0.254, 0.525, 0.756 and 1.049 μm. **d** EDS elemental mapping of 0.756 μm EZS. **e** Doped Eu content under different synthesis conditions. **f** HAADF-STEM images of an individual EZS and its rim region. **g** HR-TEM micrograph with the corresponding SAED pattern. **h** AC-HAADF-STEM microstructure and **i** atomic-scale EDS elemental mapping, **j** revealing the distribution of Zr, Eu and O atoms. **k** Zr 3*d* and **l** Eu 3*d* XPS spectra of EZS

https://doi.org/10.1007/s40820-026-02195-8

electrons at 1.0×10^{14} e cm^{-2}. UV exposure was applied using deuterium and xenon lamps with an acceleration factor of ~ 5, corresponding to 1000 equivalent solar hours. AO tests were carried out using a SimulTek CompactAO system (SimulTek Research Co., Ltd.) with an average AO energy of 5 eV and a total fluence of 1×10^{20} atoms cm^{-2}.

2.4 Density Functional Theory (DFT) Calculations

DFT calculations of Eu-doped ZrO_2 were carried out using the Vienna Ab initio Simulation Package (VASP). Ground-state electronic structures and formation energies were first obtained with the Perdew-Burke-Ernzerhof (PBE) exchange–correlation functional within the generalized gradient approximation (GGA) and projected augmented-wave (PAW) pseudopotentials [30, 31]. Eu-doped ZrO_2 was modeled using a supercell approach, with a plane-wave cutoff energy of 600 eV and a $2\times2\times3$ Monkhorst–Pack *k*-point mesh for Brillouin-zone sampling. All structures were relaxed until the residual forces on each atom were below 5×10^{-4} eV atom^{-1}. Finite-temperature electronic structures and formation energies at 300 K were evaluated using an electron–phonon coupling scheme [32]. Since GGA-PBE is known to underestimate bandgaps in systems containing correlated *d* and *f* states, the E_g and electronic structure were further refined using the HSE06 hybrid exchange–correlation functional, which provides a more reliable description of the electronic self-energy [33].

2.5 Numerical Simulation

The optical simulation was evaluated by combining Mie scattering theory and Monte Carlo (MC) ray tracing method [34–37]. For an isolated submicrosphere, the scattering (Q_{sca}), extinction (Q_{ext}) and absorption (Q_{abs}) efficiencies were obtained from classical Mie scattering theory:

$$Q_{\text{sca}}(m,\chi)=\frac{2}{\chi^2}\sum_{n=1}^{\infty}(2n+1)\left(\left|a_n\right|^2+\left|b_n\right|^2\right) \tag{1}$$

$$Q_{\text{ext}}(m,\chi)=\frac{2}{\chi^2}\sum_{n=1}^{\infty}(2n+1)\text{Re}\left\{a_n+b_n\right\} \tag{2}$$

$$Q_{\text{abs}}=Q_{\text{ext}}(m,\chi)-Q_{\text{sca}}(m,\chi) \tag{3}$$

The Mie coefficients of a_n and b_n are given by:

$$a_n=\frac{m\psi_n(m\chi)\psi_n'(\chi)-\psi_n(\chi)\psi_n'(m\chi)}{m\psi_n(m\chi)\xi_n'(\chi)-\psi_n'(m\chi)\xi_n(\chi)} \tag{4}$$

$$b_n=\frac{\psi_n(m\chi)\psi_n'(\chi)-m\psi_n(\chi)\psi_n'(m\chi)}{\psi_n(m\chi)\xi_n'(\chi)-m\xi_n(\chi)\psi_n'(m\chi)} \tag{5}$$

where ψ_n and ξ_n are Riccati-Bessel functions; $\chi=\frac{\pi D}{\lambda}$ is the size parameter; $m=\frac{n+ik}{n_0}$ is the complex refractive index normalized to the surrounding medium.

For metacoatings composed of EZS submicrospheres embedded in a K_2SiO_3 binder, assuming independent scattering, the scattering coefficient (k_{sca}) and anisotropy factor (g) were obtained by [35]:

$$k_{\text{sca}}=f_v\int_{D_1}^{D_n}k_{\text{sca}}(D)\frac{\pi D^3}{6}n(D)\text{d}D=\frac{3f_v}{2}\int_{D_1}^{D_n}Q_{sca}(D)\cdot\frac{\pi D^2}{6}n(D)\text{d}D \tag{6}$$

$$g=\int_{D_1}^{D_n}\frac{k_{\text{sca}}(D)}{k_{\text{sca}}}\int_0^{2\pi}\Phi(\theta,D)\sin\theta\cos\theta\text{d}\theta\,\frac{\pi D^3}{6}n(D)\text{d}D=\int_{D_1}^{D_n}\frac{k_{\text{sca}}(D)}{k_{\text{sca}}}g(D)\frac{\pi D^3}{6}n(D)\text{d}D \tag{7}$$

where n(D)dD is the probability density function between D and $D+\text{d}D$. The diameter distribution follows a log-normal form [38, 39]:

$$n(D)=\frac{1}{D\sigma\sqrt{2\pi}}\exp\left(-\frac{(\ln D-\mu)^2}{2\sigma^2}\right) \tag{8}$$

where (μ) and (σ) are the geometric mean diameter and geometric standard deviation, respectively.

The total backscattering strength (S_t) of a coating with thickness (H) was written as:

$$S_t=S_{\text{sca}}\cdot H=k_{\text{sca}}\cdot H\cdot(1-g)/2 \tag{9}$$

At higher volume fractions, dependent scattering effects were included via a correction factor (γ), giving:

$$S_t^{\mathrm{Dep}} = \gamma \cdot S_t \tag{10}$$

The effective radiative properties (k_{sca}, g, $S_{\mathrm{t}}^{\mathrm{Dep}}$) were then used as inputs for MC simulations of reflectance and transmittance. For each parameter set, 10^6 photons were launched at normal incidence onto a layer of prescribed thickness. Photon paths were traced through the medium by stochastically sampling free paths, scattering angles (from the phase function), and absorption events based on the extinction coefficient. Photons exiting the entrance surface were counted as reflected, whereas those leaving the back surface were counted as transmitted. The spectral reflectance $R(\lambda)$ and transmittance $T(\lambda)$ were obtained by normalizing reflected and transmitted weights to the incident total. To efficiently explore design space and identify low-α_{s} structures, the MC solver was coupled to two optimization strategies: a constrained-gradient routine for local optimization and a grid-search mapper for global scans over submicrosphere diameter, volume fraction and metacoating thickness [25].

3 Results and Discussion

3.1 Controlled Synthesis, Characterization and Modulation Fluorescence of EZS

Advancing the development of photonic metacoatings that integrate high-sensitivity fluorescence thermometry with high-performance space radiative cooling, we developed a controlled synthesis of EZS guided by our previously established oligomeric aggregation pathway [28]. Forced hydrolysis of alkoxide oligomeric precursors with concurrent Eu^{3+} coordination under hydrothermal conditions enabled precise control over both submicropshere diameter and dopant loading (Figs. S1 and S2). Diameters were tuned to 0.254, 0.525, 0.756 and 1.049 μm under the optimized calcination, as validated by scanning electron microscopy (SEM) (Figs. 1c and S3–S6). The selected diameters cover the principal solar wavelengths for Mie scattering, allowing identification of the minimum-α_s configuration of metacoating for enhanced radiative cooling. The uniformly elemental distributions of Zr, O and Eu across submicrospheres with different diameters are confirmed by energy-dispersive X-ray spectroscopy (EDS) analysis, ensuring compositionally homogeneous building blocks for constructing the photonic metacoating (Figs. 1d and S7). In parallel, Eu contents were adjusted to 1.93%, 5.23%, 8.48% and 10.81%, as verified by inductively coupled plasma optical emission spectrometry (ICP-OES), providing a compositional space to optimize fluorescence thermometric performance (Fig. 1e).

Comprehensive structural and chemical characterizations were performed on the EZS. The EZS exhibit well-defined spherical morphology composed of nanocrystallites typically smaller than 10 nm (Figs. 1f, g). Selected-area electron diffraction (SAED) confirms a polycrystalline tetragonal phase, indicated by rings corresponding to the (101), (002), (200), and (202) planes (Fig. 1g) [40]. Rietveld refinement analysis indicates that Eu is incorporated into the Zr lattice sites within the $P4_2/nmc$ crystal structure (Fig. S8). Aberration-corrected high-angle annular dark-field scanning transmission electron microscopy (AC-HAADF-STEM) imaging shows lattice fringes of 0.307 nm, matching the (101) interplanar spacing of tetragonal ZrO_2, while atomic-scale EDS mapping verifies selective substitution of Eu^{3+} at Zr sites (Fig. 1i) [41]. Although the O distribution could not be precisely mapped due to signal overlap, the periodic Zr/Eu arrangement spanning ten atomic sites shows a length of 3.074 nm, corresponding to approximately ten times the (101) lattice spacing, which confirms the homogeneous Eu incorporation (Fig. 1j). X-ray photoelectron spectroscopy (XPS) analysis further confirms the chemical states of the constituent elements (Fig. S9). The Zr 3d spectrum shows a doublet at 181.79 and 184.18 eV ($\Delta E = 2.39$ eV), consistent with the presence of Zr^{4+} in the lattice (Fig. 1k) [42, 43]. The Eu 3d spectrum displays a typical doublet at 1134.28 eV (Eu $3d_{5/2}$) and 1163.90 eV (Eu $3d_{3/2}$) with a splitting of 29.62 eV, confirming successful Eu^{3+} doping (Fig. 1l). Additional satellite peaks observed at 1124.11 and 1155.25 eV suggest enhanced 4f electron localization, plausibly arising from V_O-mediated charge-transfer processes [44, 45].

To enable non-contact fluorescence thermometry in EZS metacoatings for space radiative cooling, we systematically investigated the effects of Eu doping on the optical E_g and fluorescence behavior. DFT calculations were performed on Eu-doped or pristine ZrO_2 (Figs. 2a–c and S10). In the projected density of states (PDOS) of pristine ZrO_2, the valence band maximum (VBM) arises mainly from O 2p orbitals, while the conduction band minimum (CBM) originates from Zr 4d states [29, 46]. Upon Eu incorporation,

https://doi.org/10.1007/s40820-026-02195-8

the overall shape and position of both VB and CB remain largely unchanged, indicating that the intrinsic E_g of ZrO_2 is essentially preserved. However, sharp and localized peaks of Eu^{3+} $4f$ states emerge near the CB edge. These $4f$ orbitals, effectively shielded by outer $5s^2 5p^6$ electrons, exhibit weak hybridization with the host lattice, confining excitation energy within Eu^{3+} ions and minimizing nonradiative loss to the matrix. The localized $4f$ states thus serve as efficient optical centers, governing both absorption and emission via $4f$-$4f$ transitions. This localized-state-mediated luminescence underpins efficient fluorescence thermometry by strengthening radiative transitions without largely perturbing the E_g and increasing α_s.

Experimental optical characterizations further validate the theoretical findings. With increasing Eu doping under optimized calcination conditions, Tauc plot analysis of $(ahv)^2$ versus photon energy (hv) reveals a slight reduction in the optical E_g, consistent with DFT predictions (Figs. 2d and S11) [47]. This reduction arises primarily from the formation of V_O that accompanies Eu^{3+} substitution for Zr^{4+}. Concurrently, Fourier transform infrared (FTIR) spectra show no significant changes in chemical composition (Fig. S12). X-ray diffraction (XRD) analysis reveals a

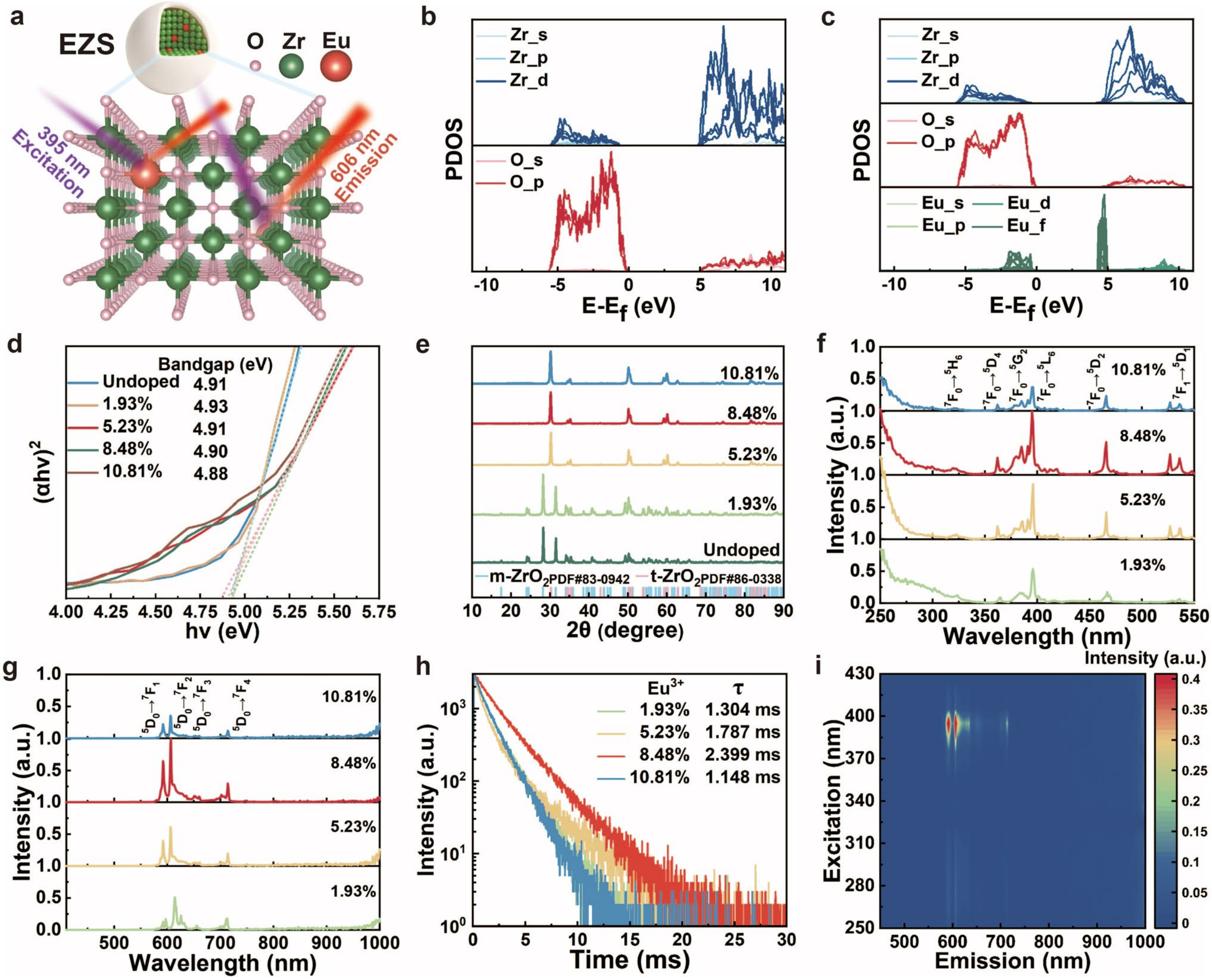

Fig. 2 Modulation of EZS optical and photoluminescent properties. **a** Tetragonal crystal structure of EZS with Eu^{3+} as luminescent centers. PDOS of **b** undoped and **c** 8.33% Eu-doped ZrO_2. **d** Optical E_g derived from Tauc plots, **e** XRD patterns, **f** excitation spectra, **g** emission spectra, **h** fluorescence decay curves ($\lambda_{em} = 606$ nm and $\lambda_{ex} = 395$ nm) at different doping concentrations and **i** excitation-emission contour map of 8.48% EZS

structural transformation from the monoclinic phase ($2\theta = 24.1°$, 28.2°, 31.5°, 34.1°, 50.2°; PDF#83-0942) to the tetragonal phase ($2\theta = 30.2°$, 35.3°, 50.2°, 60.1°; PDF#86-0338) upon Eu doping at higher concentrations (Fig. 2e) [41]. Even at a high Eu content of 8.48%, the E_g remains nearly unchanged compared with undoped ZrO_2, ensuring that the metacoating maintains its low α_s.

We further investigated the fluorescence properties, and the excitation ($\lambda_{em} = 606$ nm) and emission ($\lambda_{ex} = 395$ nm) spectra are shown in Figs. 2f, g and S13. The broad band of 250–325 nm arises from $O^{2-}(2p) \to Eu^{3+}(4f)$ charge-transfer excitation, which is intense and sensitive to local coordination. Peaks at 320, 362, 385, 395, 465 and 527 nm correspond to the Eu^{3+} $^7F_0 \to {}^5H_6$, $^7F_0 \to {}^5D_4$, $^7F_0 \to {}^5G_2$, $^7F_0 \to {}^5L_6$, $^7F_0 \to {}^5D_2$ and $^7F_1 \to {}^5D_1$ transitions [23, 48]. Emission bands at 583–600, 600–637, 645–665 and 690–720 nm correspond to $^5D_0 \to {}^7F_J$ (J = 1–4). The $^5D_0 \to {}^7F_1/{}^7F_3$ bands are magnetic dipole, while $^5D_0 \to {}^7F_2/{}^7F_4$ are electric dipole and intensify at non-centrosymmetric Eu^{3+} sites, with the splitting confirming complete lifting of the ^7F_J degeneracy [49]. With increasing Eu content, both excitation and emission first increase and then decrease, giving an optimum at 8.48%. The decay curves show the lifetime follows the same trend, initially increasing with Eu content, reaching 2.399 ms at 8.48% and falling to 1.148 ms at 10.81% (Fig. 2h). The initial enhancement is attributed to two factors: more activator ions (Eu^{3+}) per EZS directly increase emission centers and Eu substitution on Zr sites with charge-compensating V_O that break local centrosymmetry and promote energy transfer to Eu^{3+} [48]. At higher loading, over-strong charge-transfer absorption reduces the effective excitation of 4*f*-4*f* transitions, and concentration-quenching pathways such as cross-relaxation and defect-assisted nonradiative transfer dominate, reducing intensity and lifetime [49]. Undoped ZS show no detectable emission (Fig. S14), confirming that luminescence originates from Eu incorporation. The excitation-emission contour map reveals an active region spanning 385–400 nm in excitation and 580–640 nm in emission, predominantly governed by the $^7F_0 \to {}^5L_6$, $^7F_0 \to {}^5D_2$ and $^5D_0 \to {}^7F_2$ transitions (Fig. 2i). Overall, 8.48% Eu content defines the optimal composition for yielding strong red emission and maximizing luminescent performance.

3.2 Photonically Optimized Metacoatings for Minimized α_s and Enhanced Radiative Cooling Performance

Photonic structure optimization is pivotal for minimizing α_s and, in turn, maximizing radiative cooling performance. To support rational and fabrication-tolerant design, we combined a high-efficiency constrained-gradient optimization with a complementary grid-search map to chart the α_s landscape and delineate the optimal region across the EZS parameter space [25]. Using α_s minimization as the objective, the constrained-gradient routine converged to machine tolerance (e^{-10}) and returned fast, accurate optima for the EZS diameter and volume fraction. As shown in Fig. 3a, multi-start optimizations launched from four contrasting combinations (small/large diameters × low/high volume fractions) collapse to a narrow basin at diameter of 0.70–0.75 μm and volume fraction of 32%–36%, identifying a global optimum for minimizing α_s. To test global robustness and resolve response trends, we constructed a diameter-volume-fraction design grid and executed a full factorial sweep via grid search (Fig. 3b). For experimental validation, EZS metacoatings were fabricated using four representative diameters (0.254, 0.525, 0.766 and 1.049 μm) and volume fractions (15%, 25%, 35% and 45%). K_2SiO_3 was selected as the binder because its excellent optical transparency, strong irradiation resistance, water-based processability, and ability to form a robust Si–O–Si network provide key advantages for constructing stable photonic metacoatings [9]. SEM images show that the EZS are uniformly embedded and randomly dispersed within the K_2SiO_3 binder, forming a heterogeneous particulate architecture. Increasing the EZS diameter decreases the particle number density and produces a more sparsely distributed network of larger scattering centers (Figs. 3c and S15). Increasing the volume fraction from 15% to 45% progressively increases the packing density and interparticle connectivity, generating distinct photonic architectures (Fig. S16). Together, these parameters govern the size, density and spatial distribution of scattering centers within the metacoating, enabling comparative optical characterization.

Reflectance and emittance spectra under different structural parameters were conducted to evaluate optical performance. Reflectance varies with wavelength and diameter, with 0.254 μm EZS metacoating showing the highest reflectance in 0.38–0.52 μm, 0.756 μm EZS

https://doi.org/10.1007/s40820-026-02195-8

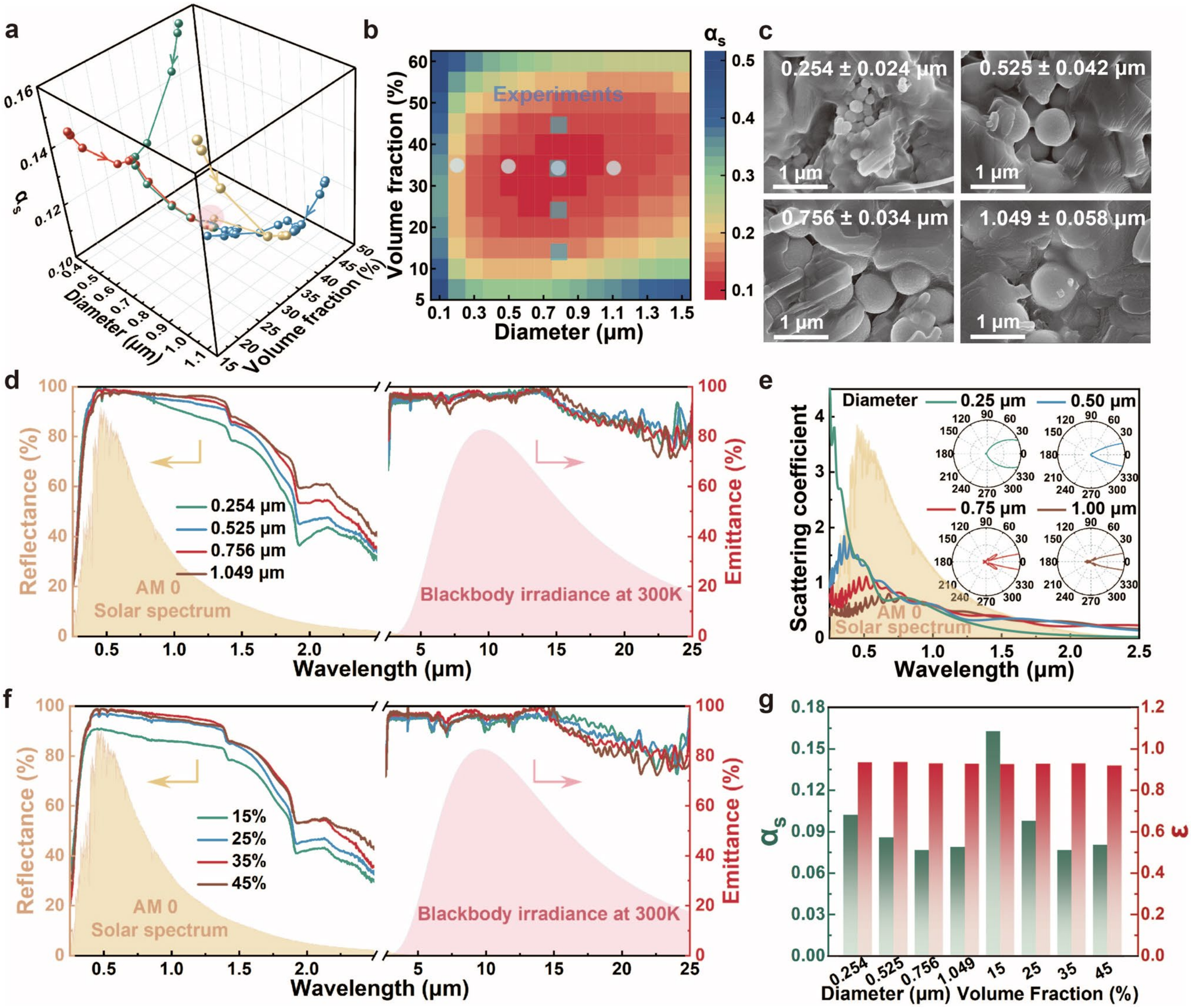

Fig. 3 Photonic structure optimization of EZS metacoating. **a** Constrained gradient optimization and **b** grid search mapping of the optimal α_s region for 100 μm thick metacoatings as a function of diameter and volume fraction. **c** SEM images, **d** reflectance and emittance spectra of metacoatings with varying EZS diameters. **e** Scattering coefficient spectra of EZS with different diameters and corresponding phase functions at 0.5 μm for incident light (inset). **f** Reflectance and emittance spectra of EZS metacoatings with different volume fractions. **g** α_s and ε of EZS metacoatings with different diameters and volume fractions

metacoating performing best in 0.52–0.87 μm, and reflectance increasing monotonically with diameter in 0.87–2.5 μm. These trends match the simulated profiles and arise from a red-shift of the scattering-efficiency maximum with increasing diameter, which enhances backscattering at longer wavelengths (Figs. 3e and S17). Phase-function analysis further confirms stronger backscattering for larger submicrospheres. Consistently, increasing the EZS diameter from 0.254 to 0.756 μm lowers α_s from 0.102 to 0.076, while a further increase to 1.049 μm yields a slight rebound to 0.079. ε shows only minor variation, remaining within 0.928–0.936 owing to the strong phonon polariton modes of K_2SiO_3 and EZS (Fig. 3g) [50, 51].

Volume fraction likewise governs the optical response. At volume fraction of 15%, the sparse scattering centers result in low broadband reflectance (Figs. 3f and S16). Raising the volume fraction to 35% increases backscattering and raises reflectance across the solar spectrum. At 45%, excessive particle crowding reduces effective scattering interfaces and depresses reflectance in the 0.54–1.37 μm region, in agreement with simulated results (Figs. 3f and S17). Accordingly, α_s drops from 0.163 to 0.076 as the volume fraction increases from 15% to 35%, while ε rises from 0.926 to 0.931. When the fraction reaches 45%, α_s slightly increases to 0.081 and ε declines to 0.920, underscoring that excessive loading compromises performance (Fig. 3g). As the thickness increases, the α_s first decreases and then remains nearly constant with slight fluctuations (Fig. S18). Specifically, increasing the metacoating thickness from 50 to 100 µm reduces α_s from 0.106 to 0.076 due to enhanced photon backscattering. Further thickening leads to only marginal changes, with α_s reaching 0.075 at 200 µm and slightly increasing to 0.077 at 300 µm due to increased near-infrared absorption in the K_2SiO_3 binder. Meanwhile, the ε gradually increases from 0.914 to 0.945 with thickness. Since further thickening beyond 100 µm provides limited optical benefits while increasing metacoating weight and cracking risk, a thickness of approximately 100 µm was selected as a practical optimum. In summary, for a ~ 100 µm-thick metacoating, an EZS diameter of 0.756 µm and a volume fraction of 35% yield a minimum α_s of 0.076 while maintaining a high ε of 0.931.

The metacoating can be readily scaled up and fabricated using an industrially compatible spray process, producing a 0.5 m × 0.5 m metacoating that maintains excellent optical uniformity and random structural characteristics (Fig. 4a). Cross-sectional SEM images taken at the top, middle and bottom regions of the ~ 100 µm thick metacoating show similar microstructures with randomly dispersed EZS in the K_2SiO_3 matrix, indicating a uniform structure without observable gradient features (Fig. 4b). EDS analysis confirms the compositional uniformity of the metacoating. The Zr and O signals delineate the EZS domains, while Eu shows a diffuse distribution due to its low doping concentration. Si is uniformly distributed, indicating the formation of a continuous three-dimensional silicate network, whereas slight local enrichment of K likely originates from K_2SiO_3 condensation (Fig. 4c). Infrared thermal imaging shows that the K_2SiO_3, EZS and metacoating appear markedly hotter than the surrounding bare Al, indicating high apparent emissivity arising from strong mid-infrared Si–O and Zr–O vibrations (Fig. 4d) [9]. Concurrently, the metacoating exhibits bright, uniform red luminescence from the $Eu^{3+}\ {}^5D_0 \rightarrow {}^7F_2$ transition under 395 nm excitation (Fig. 4e).

To evaluate the radiative cooling performance of the EZS metacoating, we first compared its net cooling power with commercial and reported counterparts. As shown in Fig. 4f and Table S1, the EZS metacoating attains a maximum net cooling power of 323.69 W m^{-2}, enabled by its ultralow α_s and ε, surpassing state-of-the-art counterparts that typically remain below 300 W m^{-2}. In comparison, the widely used AZ-93 and YB-71 coatings, formulated with ZnO and Zn_2TiO_4 pigments, deliver net cooling powers of 212.89 and 253.79 W m^{-2}, respectively. Their cooling performance is primarily limited by higher α_s, which increases solar energy uptake and reduces overall cooling efficiency. Then the radiative cooling performance was tested in a vacuum chamber with a black-coated interior as the cold sink (Fig. 4g). To simulate the spacecraft thermal environment, each coated Al sheet was subjected to stable AM0 solar radiation (1367 W m^{-2}) via a quartz window and fitted with a resistive heater, mimicking both solar exposure and internal heat generation (Fig. S19). Three independent measurements yielded standard deviations below 0.3 °C for the EZS metacoating and below 1 °C for the Al sheet, confirming the high stability of the testing system and the excellent reproducibility of the measurements (Fig. S20). Under AM0 solar illumination and 395 nm excitation, the EZS metacoating exhibits a bright irradiance spot and uniform red luminescence in Fig. 4h. For benchmarking, we compared it with TiO_2 ($\alpha_s = 0.184$, $\varepsilon = 0.901$), ZnO ($\alpha_s = 0.155$, $\varepsilon = 0.948$) and Zn_2TiO_4 ($\alpha_s = 0.147$, $\varepsilon = 0.939$) coatings, which represent the principal pigment systems used in above commercial all-inorganic radiative cooling coatings (Figs. S21 and S22) [29]. After 40 min of solar exposure, the EZS metacoating stabilizes at 28.1 °C, which is 16.6 °C cooler than bare Al sheet and cooler than TiO_2, ZnO and Zn_2TiO_4 coatings by 7.3, 4.4 and 3.8 °C, respectively (Fig. 4i). With a 2 W internal heat load alone, the oxide-based coatings exhibit similar temperatures because their emittances are comparable, whereas the Al sheet heats rapidly due to its low ε. Under simultaneous solar exposure and internal heating, the EZS metacoating remains the top performer, operating 77.0 °C below bare Al and cooler than TiO_2, ZnO and Zn_2TiO_4 coatings by 9.1, 5.2 and 3.8 °C. This superiority stems from its favorable photothermal balance ($\alpha_s = 0.076$, $\varepsilon = 0.931$) and the optimized photonic architecture of the submicrosphere, which strengthens multiple backscattering to reject solar input while maintaining strong thermal emission to dissipate heat, thereby enabling highly efficient radiative cooling.

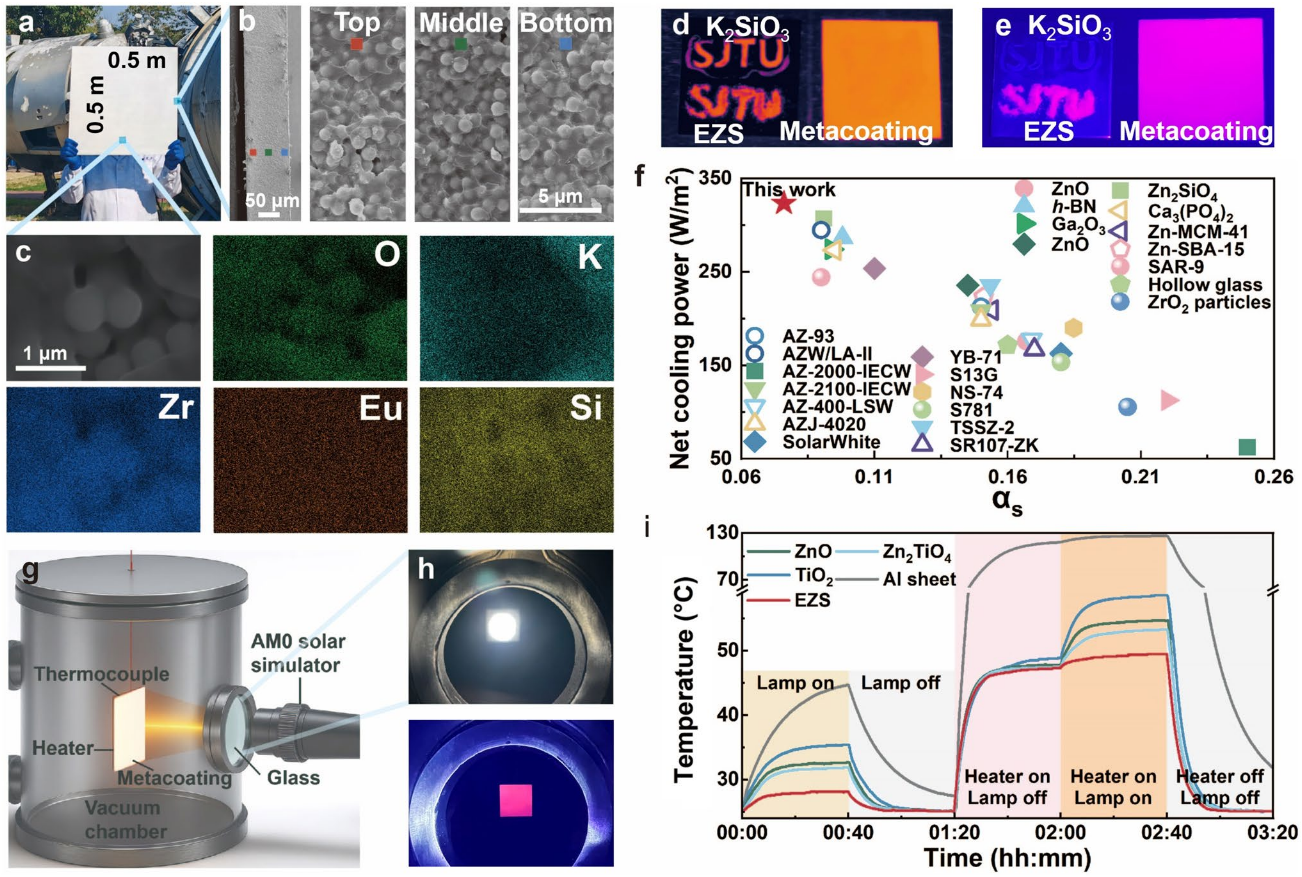

Fig. 4 Structural, optical and radiative cooling characterization of the EZS metacoating. **a** Photograph (0.5 m×0.5 m), **b** cross-sectional and **c** surface SEM images of EZS metacoating with corresponding EDS elemental mapping, showing about 100 μm thickness and homogeneous EZS dispersion. **d** Infrared thermal image after thermal equilibrium at 50 °C and **e** optical photograph under 395 nm excitation for EZS, K_2SiO_3 and the metacoating on an Al sheet. **f** Comparison of net cooling power between the EZS metacoating and other all-inorganic radiative cooling coatings across varying α_s. **g** Schematic of the vacuum experimental setup simulating space conditions. **h** EZS metacoating under AM0 illumination and 395 nm excitation. **i** Temperature evolution of the EZS metacoating, Al sheet, and reference coatings during lamp on–off cycles, with and without heater input

3.3 Fluorescence Thermometry of EZS Metacoatings

To assess the thermometric capability of EZS metacoatings, we measured temperature-dependent luminescence from 173 to 433 K. Under 395 nm excitation, the spectra display the characteristic Eu^{3+} emission bands (Fig. 5a). The integrated intensity decreases monotonically with increasing temperature, consistent with thermally activated nonradiative relaxation that lowers the radiative recombination efficiency (Fig. S23). In parallel, millisecond lifetimes indicate intrinsically low nonradiative decay, and their continuous shortening from 2.167 ms at 173 K to 1.543 ms at 423 K attests to the growing dominance of thermal quenching (Fig. 5b) [52]. The concurrence of a long baseline lifetime with pronounced thermal dependence is a hallmark of high-quality thermometric phosphors and underpins high signal-to-noise and sensitivity.

We further implemented FIR thermometry by using the intensity ratio I_{548}/I_{606}, corresponding to the $^5D_1 \rightarrow {}^7F_2$ and $^5D_0 \rightarrow {}^7F_2$ transitions, taking advantage of the stronger thermal quenching of the hypersensitive 606 nm line relative to the 548 nm emission, which generates a robust temperature-dependent fluorescence ratio. The FIR increases exponentially with temperature and is well described by a modified Boltzmann fit ($R^2 = 0.9941$, Fig. 5c). The absolute sensitivity S_a rises to 0.0134 K^{-1} at 433 K, while the relative sensitivity S_r peaks at 0.797% K^{-1} at 353 K, indicating high resolution in the mid-temperature range and robust detectability at elevated temperatures (Fig. 5d). Benchmarking against reported thermometric oxides shows that the wide E_g of EZS shortens the λ_g and supports a low α_s of metacoating (Fig. 5e and Table S2). The EZS metacoating achieves higher S_r than materials with comparable or shorter λ_g (S_r typically below 0.55% K^{-1}) and outperforms most high-λ_g systems, demonstrating its superior thermometric sensitivity and the effectiveness of a concurrently optimized material-structure strategy. Taken together, the results demonstrate broadband temperature responsiveness and high sensitivity over 173–433 K, highlighting the practical promise of low-α_s EZS metacoatings for integrated, non-contact optical thermometry and space radiative cooling.

3.4 Irradiation Resistance in Extreme Space Environments

The suitability of a metacoating for long-term on-orbit service hinges on its resilience to space stressors, so post-irradiation optical stability is a primary metric. We measured the reflectance and emittance of the EZS metacoating after proton, electron, AO, UV and combined exposures (Figs. 6a, b). Proton and AO cause only slight losses in 0.25–0.70 μm with minimal color change. Electron caused a pronounced reflectance to drop in the 0.38–0.70 μm range and produced a gray tint, indicating the formation of color centers that absorb visible light as a result of irradiation-induced lattice damage. UV irradiation produces a marked reflectance drop across 0.25–1.38 μm together with a light ochre tint, attributable to photoinduced charging and the creation of surface states that increase absorption. The metacoating exhibits surface coarsening and locally fragmented features after UV and combined irradiations (Fig. S24), likely arising from photo-induced bond scission within the silicate network. Nevertheless, the matrix remains continuous and effectively anchors the EZS. Across all cases, changes in the infrared are minor. Consistently, the α_s shifts from 0.076 to 0.090 (proton), 0.110 (electron), 0.088 (AO), 0.159 (UV) and 0.174 (combined irradiations), while the ε is essentially unchanged with variations below 0.01 (Fig. 6c).

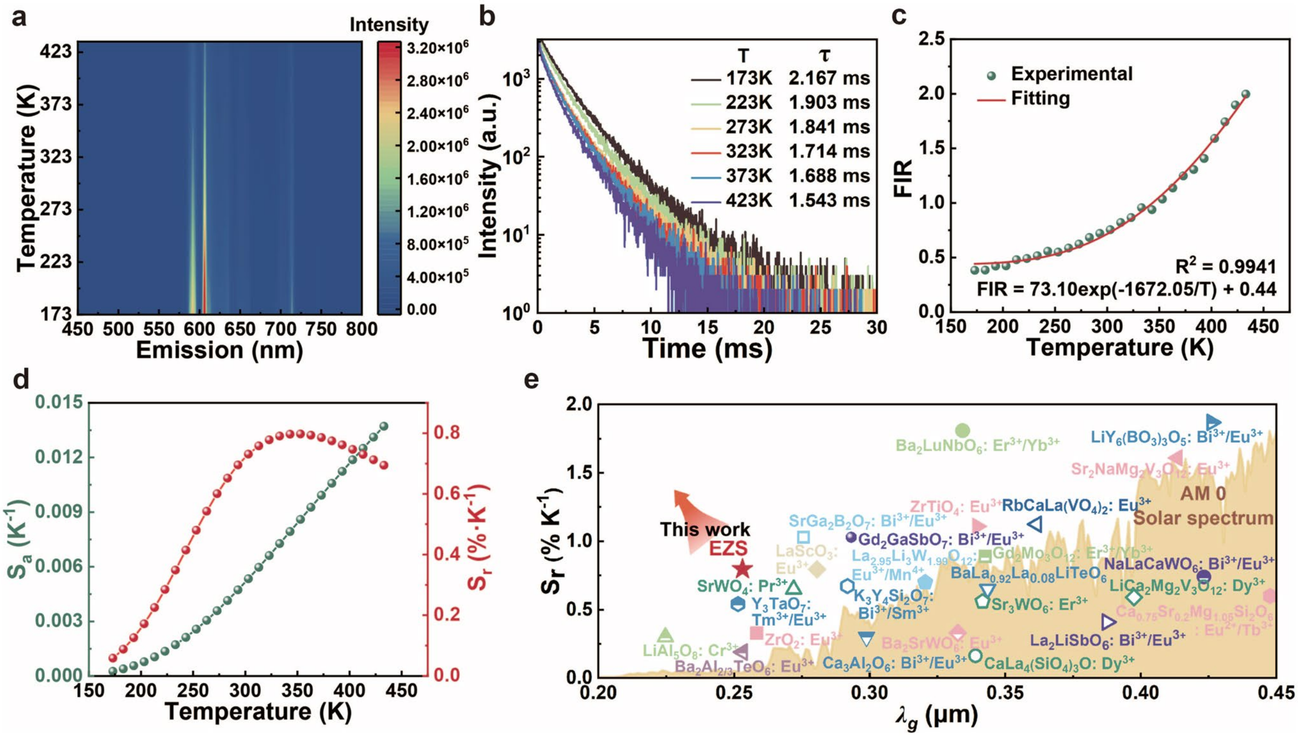

Fig. 5 Temperature-dependent luminescence and thermometric performance of EZS metacoating. **a** Temperature-dependent emission spectra and **b** fluorescence decay curves of EZS under 395 nm excitation. **c** Variation of FIR (I_{548}/I_{606}) with temperature. **d** S_a and S_r. **e** Comparison of λ_g and maximum S_r for the EZS metacoating and representative luminescent thermometric oxide

https://doi.org/10.1007/s40820-026-02195-8

Although the α_s increases noticeably after UV and combined irradiations, the metacoating still delivers net cooling powers of 206.55 and 185.59 W m^{-2} at 300 K, respectively, demonstrating that effective radiative cooling performance is retained. Thermal cycling is equally critical for space reliability. After 50, 100, and 150 thermal cycles between -196 and 150 °C, the α_s increases by 0.009, 0.016, and 0.032, and ε decreases by 0.002, 0.007, and 0.015, accompanied by gradually enlarged microcracks, while the optical properties remain largely stable, demonstrating good thermal shock tolerance (Figs. 6d, S25, and S26).

A comparative evaluation with representative radiative cooling coatings demonstrates that the EZS metacoating maintains the lowest α_s in the cohort before and after electron, proton, AO, UV and combined exposures (Fig. 6h and Table S3). In particular, compared with the widely used AZ-93 and YB-71 coatings, the EZS metacoating preserves an α_s advantage exceeding 0.04 even after proton, AO and UV irradiations. Meanwhile, the fluorescence thermometric performance remains well preserved after combined irradiations, with a maximum temperature deviation below 6.1%, owing to the intrinsic robustness of FIR thermometry and the high spectral stability of Eu^{3+} emissions (Fig. S27). Pull-off tests reveal strong adhesion between the EZS metacoating and the Al sheet, with strengths of 2.2 and 1.5 MPa before and after combined irradiations, respectively (Fig. S28). SEM images further confirm a stable interface between metacoating and Al sheet without noticeable delamination after combined irradiations, demonstrating stable adhesion and structural integrity (Fig. S29). These findings confirm that the EZS metacoating possesses exceptional irradiation resistance, sustaining its low α_s, high ε and stable fluorescence thermometry under multiple space stressors, thereby underscoring its strong potential for long-term and stable spacecraft thermal management.

Optical changes following irradiations primarily originate from defect formation. We employed electron paramagnetic resonance (EPR) spectroscopy to analyze the EZS metacoating before and after exposure to proton, electron, AO and UV irradiations (Fig. 6e). The pristine metacoating exhibits two anisotropic signals at $g_{\perp} = 1.9751$ and $g_{\parallel} = 1.9598$, consistent with a low concentration of Zr^{3+} centers, along with an isotropic signal at $g = 2.0027$ characteristic of singly charged V_O. After proton and AO irradiations, the intensities of both the Zr^{3+} and V_O signals increase slightly, suggesting the formation of defects at relatively low concentrations. This limited defect generation is consistent with the small increase in α_s observed after these irradiations. In contrast, electron and UV irradiations generate a rhombic triplet at $g_{zz}= 2.0142$, $g_{yy} = 2.0048$, $g_{xx} = 1.9947$ and $g_{zz} = 2.0152$, $g_{yy} = 2.0059$, $g_{xx} = 1.9956$, characteristic of O^{-} centers [53, 54]. These g-tensors arise when holes created by excitation of valence-band electrons are trapped by lattice O^{2-} under irradiation [55]. The formation of these defect centers introduces localized E_g states that act as color centers and enhance solar absorption, while the stronger EPR signal intensity observed after UV irradiation compared with electron irradiation indicates a higher defect concentration, consistent with the more pronounced increase in α_s.

XPS characterization further corroborates the EPR findings. In the Zr 3d region, the pristine metacoating shows Zr^{4+} peaks at 181.26 eV (3$d_{5/2}$) and 183.63 eV (3$d_{3/2}$) with a spin–orbit splitting of ~ 2.37 eV (Fig. 6f). Proton and AO exposures induce minor binding energy shifts. In contrast, electron and UV irradiations shift the Zr 3d doublet to 182.22 and 184.57 eV while maintaining Zr^{4+} character (splitting ~ 2.35 eV), suggesting a net reduction of electron density due to nearby defect-charge rearrangement. The Eu 3d spectra display characteristic Eu^{3+} peaks at 1134.27 and 1164.01 eV ($\Delta E = 29.59$ eV) in Fig. 6g, accompanied by satellites at 1124.45 and 1154.04 eV reflecting enhanced 4f localization [44, 45]. While proton and AO irradiations cause only negligible spectral changes, electron and UV exposures shift the Eu 3d peaks to 1134.58/1164.09 and 1133.72/1163.72 eV, respectively, accompanied by a near disappearance of the satellite features. The suppression of these satellites indicates partial delocalization of Eu^{3+} 4f electrons and the participation of Eu^{3+} 4f states in irradiation-induced charge-transfer processes. Despite these electronic perturbations, the modest energy shifts confirm that Eu remains predominantly in the trivalent state, suggesting that irradiation alters the local electronic environment rather than the oxidation state. Similar perturbations are observed in O, K and Si spectra, consistent with local bonding rearrangements (Fig. S30). Meanwhile, FTIR and XRD show no discernible changes, confirming the phase and chemical composition remain essentially intact (Fig. S31).

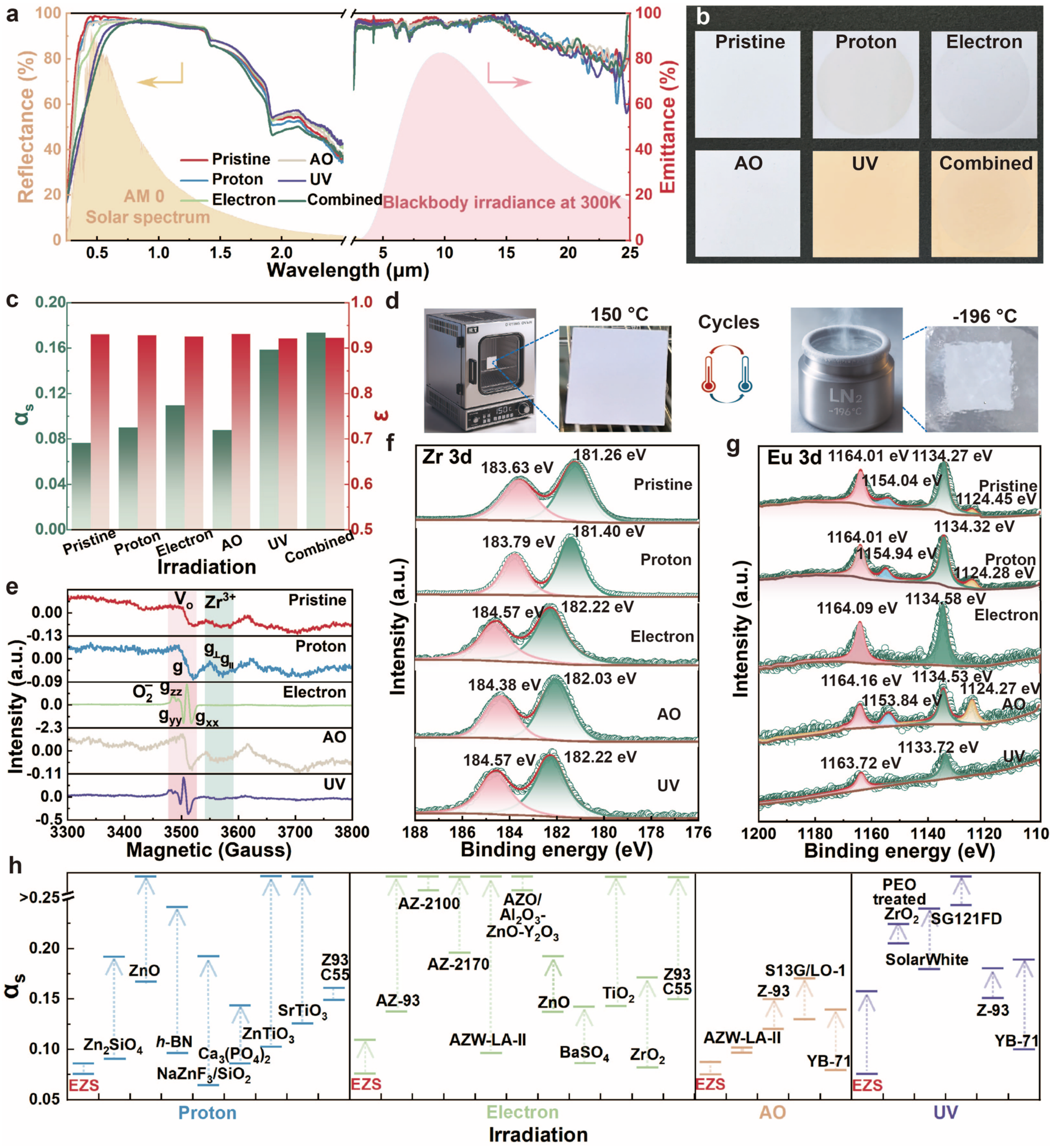

Fig. 6 Irradiation resistance of the EZS metacoating under simulated space environments. **a** Reflectance and emittance spectra, **b** photographs of 4 cm×4 cm samples and **c** comparison of α_s and ε before and after different irradiations. **d** Schematic and photographs after thermal cycles between -196 and 150 °C. **e** EPR spectra, **f** Zr 3*d* and **g** Eu 3*d* XPS spectra of the EZS metacoating before and after different irradiations. **h** Post-irradiation α_s comparison of EZS metacoating with other all-inorganic radiative cooling coatings after different irradiations

https://doi.org/10.1007/s40820-026-02195-8

4 Conclusions

In summary, we have demonstrated a dual-functional photonic EZS metacoating that integrates high-performance space radiative cooling with high-sensitivity fluorescence thermometry. Guided by photonic-scattering optimization and supported by controlled synthesis of tetragonal EZS with independently tuned diameter and Eu content, the optimal configuration with 8.48% Eu doping, 0.756 μm diameter and 35% volume fraction, achieves strong Eu^{3+}-centered emission and minimal α_s. Combined DFT and experimental analyses reveal that localized Eu^{3+} $4f$ states govern efficient luminescence without largely narrowing the E_g, maintaining low α_s. The resulting metacoating exhibits $\alpha_s = 0.076$ and $\varepsilon = 0.931$, yielding a net cooling power of 323.69 W m^{-2}. Under simulated vacuum space conditions, it reduces the temperature of an Al sheet by approximately 77 °C and operates 9.1, 5.2 and 3.8 °C cooler than TiO_2, ZnO and Zn_2TiO_4 coatings, respectively. Its fluorescence enables contactless temperature sensing over a wide range of 173–433 K, exhibiting a maximum absolute sensitivity of $S_a = 0.0134$ K^{-1} and a relative sensitivity of $S_r = 0.797\%$ K^{-1}. The wide E_g of EZS, together with the large Stokes shift of Eu^{3+} emission, ensures reliable thermometric operation under AM0 illumination without compromising radiative cooling performance. The metacoating maintains the lowest α_s and a stable ε after proton, electron, AO, UV and combined irradiations, outperforming commercial and literature-reported coatings and underscoring its irradiation resistance, while EPR/XPS analyses attribute the slight coloration to V_O and O^- defects. Collectively, the EZS metacoating, combining radiative heat rejection, self-perceptive temperature readout and irradiation robustness, provides a scalable and durable platform for intelligent spacecraft thermal management, offering a blueprint for coatings capable of autonomously monitoring and regulating thermal loads in orbit.

Acknowledgements The authors acknowledge funding from the National Natural Science Foundation of China (Grant Nos. U23A20565, 52572077), Innovation Program of Shanghai Municipal Education Commission (Grant No. 2023ZKZD15), and the Startup Fund for Young Faculty at Shanghai Jiao Tong University (Grant Nos. WH220405009, 24X010502884).

Author Contributions Hao Gong: Conceptualization, Investigation, Original draft writing, Review, Editing. Zhongyang Wang, Xiao Zhou: Conceptualization, Investigation, Supervision, Writing, Review, Editing, Funding acquisition. Yan Zheng, Liping Tong, Hongchao Li, Zhiyuan Zhao, Junjia Liu, Gang Liu: Investigation, Visualization. Tongxiang Fan: Supervision, Review, Funding acquisition.

Declarations

Conflict of interest The authors declare no interest conflict. They have no known competing financial interests or personal relationships that could have appeared to influence the work reported in this paper.

Supplementary Information The online version contains supplementary material available at https://doi.org/10.1007/s40820-026-02195-8.

References

1. A. Aili, J. Choi, Y.S. Ong, Y. Wen, The development of carbon-neutral data centres in space. Nat. Electron. **8**(11), 1016–1026 (2025). https://doi.org/10.1038/s41928-025-01476-1
2. Y. Fan, H. Chen, X. Liu, Y. Zhao, Y. Huang et al., Radiative cooling in outer space: fundamentals, advances in materials and applications, and perspectives. Adv. Mater. **37**(43), e06795 (2025). https://doi.org/10.1002/adma.202506795
3. J. Xu, W. Xie, H. Han, C. Xiao, J. Li et al., Radiative cooling materials for extreme environmental applications. Nano-Micro Lett. **17**(1), 324 (2025). https://doi.org/10.1007/s40820-025-01835-9
4. Y. Dong, B. Tian, C. Wang, G. Zhang, F. Hua et al., Dynamic radiative cooling: mechanisms, strategies, and applications for smart thermal management. Nano-Micro Lett. **18**(1), 146 (2026). https://doi.org/10.1007/s40820-025-01981-0
5. A.-Q. Xie, H. Qiu, W. Jiang, Y. Wang, S. Niu et al., Recent advances in spectrally selective daytime radiative cooling materials. Nano-Micro Lett. **17**(1), 264 (2025). https://doi.org/10.1007/s40820-025-01771-8
6. B. Gao, X. Jia, X. Wang, H. Kang, S. Lu et al., Synthesis of high solar reflectance hierarchical porous thermal control

coating *via* alkali-induced assembly for spacecraft. Mater. Today Phys. **58**, 101850 (2025). https://doi.org/10.1016/j.mtphys.2025.101850

7. J. Lv, J. Xie, N. Vitaly, Development of Zn_2SiO_4 and hexagonal BN inorganic thermal-control coatings with novel thermophysical property. Int. J. Heat Mass Transf. **218**, 124791 (2024). https://doi.org/10.1016/j.ijheatmasstransfer.2023.124791
8. Y. Xiao, A. Feng, J. Chen, Q. Cao, L. Mi et al., $MgGa_2O_4$-based thermal control coating: an ultra-low solar absorption coating with high irradiation stability. Ceram. Int. **50**(18), 33480–33487 (2024). https://doi.org/10.1016/j.ceramint.2024.06.163
9. H. Gong, Z. Wang, X. Song, H. Li, K. Sun et al., Zirconia submicrosphere/potassium silicate metacoating with high irradiation stability for radiative cooling. Adv. Compos. Hybrid Mater. **8**(1), 106 (2025). https://doi.org/10.1007/s42114-024-01130-y
10. C.D.S. Brites, R. Marin, M. Suta, A.N. Carneiro Neto, E. Ximendes et al., Spotlight on luminescence thermometry: basics, challenges, and cutting-edge applications. Adv. Mater. **35**(36), e2302749 (2023). https://doi.org/10.1002/adma.202302749
11. H. Suo, X. Zhao, Z. Zhang, Y. Wang, J. Sun et al., Rational design of ratiometric luminescence thermometry based on thermally coupled levels for bioapplications. Laser Photonics Rev. **15**(1), 2000319 (2021). https://doi.org/10.1002/lpor.202000319
12. J. Zhou, B. del Rosal, D. Jaque, S. Uchiyama, D. Jin, Advances and challenges for fluorescence nanothermometry. Nat. Methods **17**(10), 967–980 (2020). https://doi.org/10.1038/s41592-020-0957-y
13. F. Jahanbazi, Y. Mao, Recent advances on metal oxide-based luminescence thermometry. J. Mater. Chem. C **9**(46), 16410–16439 (2021). https://doi.org/10.1039/d1tc03455c
14. C. Alexander, Z. Guo, P.B. Glover, S. Faulkner, Z. Pikramenou, Luminescent lanthanides in biorelated applications: from molecules to nanoparticles and diagnostic probes to therapeutics. Chem. Rev. **125**(4), 2269–2370 (2025). https://doi.org/10.1021/acs.chemrev.4c00615
15. K. Zheng, K.Y. Loh, Y. Wang, Q. Chen, J. Fan et al., Recent advances in upconversion nanocrystals: expanding the kaleidoscopic toolbox for emerging applications. Nano Today **29**, 100797 (2019). https://doi.org/10.1016/j.nantod.2019.100797
16. A. Gu, G.-H. Pan, H. Wu, L. Zhang, L. Zhang et al., Microstructure and photoluminescence of $ZrTiO_4$: Eu^{3+} phosphors: host-sensitized energy transfer and optical thermometry. Chemosensors **10**(12), 527 (2022). https://doi.org/10.3390/chemosensors10120527
17. A. Bindhu, J.I. Naseemabeevi, S. Ganesanpotti, Vibrationally induced photophysical response of $Sr_2NaMg_2V_3O_{12}$: Eu^{3+} for dual-mode temperature sensing and safety signs. Adv. Photonics Res. **3**(6), 2100159 (2022). https://doi.org/10.1002/adpr.202100159
18. Y. Chen, J. Chen, Y. Luo, Q. Wang, H. Guo, Ba_2LuNbO_6: Er^{3+}, Yb^{3+} up-conversion phosphors for dual-mode thermometry based on fluorescence intensity ratio. J. Am. Ceram. Soc. **107**(12), 8246–8255 (2024). https://doi.org/10.1111/jace.20058
19. X. Fan, L. Xu, W. Liu, F. Yin, J. Xu et al., Energy transfer in dual-emission $LiY_6(BO_3)_3O_5$: Bi^{3+}, Eu^{3+} phosphors for temperature sensing applications. Ceram. Int. **50**(18), 32583–32590 (2024). https://doi.org/10.1016/j.ceramint.2024.06.066
20. X. Shi, Y. Chen, G. Li, K. Qiang, Q. Mao et al., Designing a dual-wavelength excitation Eu^{3+}/Mn^{4+} Co-doped phosphors for high-sensitivity luminescence thermometry. Ceram. Int. **49**(12), 20839–20848 (2023). https://doi.org/10.1016/j.ceramint.2023.03.217
21. A.A. Nashivochnikov, A.I. Kostyukov, M.I. Rakhmanova, S.V. Cherepanova, V.N. Snytnikov, Photoluminescence and structure evolution of laser synthesized ZrO_2: Eu^{3+} nanopowders depending on the dopant concentration. Ceram. Int. **49**(3), 5049–5057 (2023). https://doi.org/10.1016/j.ceramint.2022.10.018
22. M.D. Chambers, D.R. Clarke, Doped oxides for high-temperature luminescence and lifetime thermometry. Annu. Rev. Mater. Res. **39**, 325–359 (2009). https://doi.org/10.1146/annurev-matsci-112408-125237
23. A.A. Nashivochnikov, A.I. Kostyukov, A.V. Zhuzhgov, M.I. Rakhmanova, S.V. Cherepanova et al., Shaping the photoluminescence spectrum of ZrO_2: Eu^{3+} phosphor in dependence on the Eu concentration. Opt. Mater. **121**, 111620 (2021). https://doi.org/10.1016/j.optmat.2021.111620
24. H. Li, X. Song, H. Gong, L. Tong, X. Zhou et al., Prediction of optical properties in particulate media using double optimization of dependent scattering and particle distribution. Nano Lett. **24**(1), 287–294 (2024). https://doi.org/10.1021/acs.nanolett.3c03914
25. X. Song, H. Li, H. Gong, X. Liu, M. Zhang et al., Machine learning prediction framework for tailoring the optical response of particulate media. ACS Photonics **12**(5), 2775–2786 (2025). https://doi.org/10.1021/acsphotonics.5c00364
26. X.-Q. Yu, F. Li, J. Wang, N. Zhang, G.-X. Li et al., Scalable-designed photonic metamaterial for color-regulating passive daytime radiative cooling. Nano-Micro Lett. **18**(1), 153 (2026). https://doi.org/10.1007/s40820-025-01975-y
27. L. Lei, T. Wu, S. Shi, Y. Si, C. Zhi et al., Engineered radiative cooling systems for thermal-regulating and energy-saving applications. Nano-Micro Lett. **18**(1), 21 (2025). https://doi.org/10.1007/s40820-025-01859-1
28. H. Gong, X. Song, H. Li, L. Tong, Z. Wang et al., Controllable synthesis of monodispersed zirconia submicrospheres based on oligomer aggregation mechanism for enhanced scattering manipulation. Small Methods **9**(7), 2401990 (2025). https://doi.org/10.1002/smtd.202401990
29. H. Gong, L. Tong, Z. Wang, X. Song, H. Li et al., Material and structure tailored La-doped ZrO_2 submicrosphere metacoatings for high-performance space radiative cooling. Adv. Funct. Mater. (2026). https://doi.org/10.1002/adfm.202528343

30. G. Kresse, D. Joubert, From ultrasoft pseudopotentials to the projector augmented-wave method. Phys. Rev. B **59**(3), 1758–1775 (1999). https://doi.org/10.1103/physrevb.59.1758
31. J.P. Perdew, K. Burke, M. Ernzerhof, Generalized gradient approximation made simple. Phys. Rev. Lett. **77**(18), 3865–3868 (1996). https://doi.org/10.1103/physrevlett.77.3865
32. G. Kresse, J. Furthmüller, Efficiency of ab-initio total energy calculations for metals and semiconductors using a plane-wave basis set. Comput. Mater. Sci. **6**(1), 15–50 (1996). https://doi.org/10.1016/0927-0256(96)00008-0
33. L. Tong, N. Xu, H. Li, L. Yang, Z. Wang et al., Investigation of thermal control in phase-changing ABO_3 perovskites via first-principles predictions: general mechanism of emittance. Phys. Chem. Chem. Phys. **25**(10), 7302–7311 (2023). https://doi.org/10.1039/D3CP01493B
34. H. Ma, L. Wang, S. Dou, H. Zhao, M. Huang et al., Flexible daytime radiative cooling enhanced by enabling three-phase composites with scattering interfaces between silica microspheres and hierarchical porous coatings. ACS Appl. Mater. Interfaces **13**(16), 19282–19290 (2021). https://doi.org/10.1021/acsami.1c02145
35. Z. Huang, X. Ruan, Nanoparticle embedded double-layer coating for daytime radiative cooling. Int. J. Heat Mass Transf. **104**, 890–896 (2017). https://doi.org/10.1016/j.ijheatmasstransfer.2016.08.009
36. J. Peoples, X. Li, Y. Lv, J. Qiu, Z. Huang et al., A strategy of hierarchical particle sizes in nanoparticle composite for enhancing solar reflection. Int. J. Heat Mass Transf. **131**, 487–494 (2019). https://doi.org/10.1016/j.ijheatmasstransfer.2018.11.059
37. L. Wang, S.L. Jacques, L. Zheng, MCML: Monte Carlo modeling of light transport in multi-layered tissues. Comput. Methods Programs Biomed. **47**(2), 131–146 (1995). https://doi.org/10.1016/0169-2607(95)01640-f
38. W.E. Vargas, A. Amador, G.A. Niklasson, Diffuse reflectance of TiO_2 pigmented paints: spectral dependence of the average pathlength parameter and the forward scattering ratio. Opt. Commun. **261**(1), 71–78 (2006). https://doi.org/10.1016/j.optcom.2005.11.059
39. X. Xue, M. Qiu, Y. Li, Q.M. Zhang, S. Li et al., Creating an eco-friendly building coating with smart subambient radiative cooling. Adv. Mater. **32**(42), e1906751 (2020). https://doi.org/10.1002/adma.201906751
40. A. Yurdakul, H. Gocmez, One-step hydrothermal synthesis of yttria-stabilized tetragonal zirconia polycrystalline nanopowders for blue-colored zirconia-cobalt aluminate spinel composite ceramics. Ceram. Int. **45**(5), 5398–5406 (2019). https://doi.org/10.1016/j.ceramint.2018.11.240
41. A. Auxéméry, G. Philippot, M.R. Suchomel, D. Testemale, C. Aymonier, Stabilization of tetragonal zirconia nanocrystallites using an original supercritical-based synthesis route. Chem. Mater. **32**(19), 8169–8181 (2020). https://doi.org/10.1021/acs.chemmater.0c01550
42. X. Zheng, P. Yu, Y. Liu, Y. Ma, Y. Cao et al., Efficient hydrogenation of methyl palmitate to hexadecanol over Cu/m-ZrO_2 catalysts: synergistic effect of Cu species and oxygen vacancies. ACS Catal. **13**(3), 2047–2060 (2023). https://doi.org/10.1021/acscatal.2c06151
43. S. Fu, C. Hu, J. Li, H. Cui, Y. Liu et al., Tuning the crystalline and electronic structure of ZrO_2 via oxygen vacancies and nano-structuring for polysulfides conversion in lithium-sulfur batteries. J. Energy Chem. **88**, 82–93 (2024). https://doi.org/10.1016/j.jechem.2023.09.003
44. J.Y. Park, C.G. Lee, H.W. Seo, D.-W. Jeong, M.Y. Kim et al., Structural and optical properties of ZnSe: Eu/ZnS quantum dots depending on interfacial residual europium. Appl. Surf. Sci. **429**, 225–230 (2018). https://doi.org/10.1016/j.apsusc.2017.09.018
45. E. Wang, L. Li, J.-Y. Zou, S.-Y. You, R.-J. Hu et al., Regulating the energy level of a ratiometric luminescent europium(III) metal–organic framework sensor with smartphone assistance for real-time and visual detection of carcinoid biomarker. Inorg. Chem. **64**(8), 3930–3940 (2025). https://doi.org/10.1021/acs.inorgchem.4c05180
46. E.R. Khattab, S.S. Abd El Rehim, W.M.I. Hassan, T.S. El-Shazly, Band structure engineering and optical properties of pristine and doped monoclinic zirconia (m-ZrO_2): density functional theory theoretical prospective. ACS Omega **6**(44), 30061–30068 (2021). https://doi.org/10.1021/acsomega.1c04756
47. P. Makuła, M. Pacia, W. Macyk, How to correctly determine the band gap energy of modified semiconductor photocatalysts based on UV–vis spectra. J. Phys. Chem. Lett. **9**(23), 6814–6817 (2018). https://doi.org/10.1021/acs.jpclett.8b02892
48. G.-H. Pan, L. Zhang, H. Wu, X. Qu, H. Wu et al., On the luminescence of Ti^{4+} and Eu^{3+} in monoclinic ZrO_2: high performance optical thermometry derived from energy transfer. J. Mater. Chem. C **8**(13), 4518–4533 (2020). https://doi.org/10.1039/C9TC06992E
49. J. Zhou, R. Lei, H. Wang, Y. Hua, D. Li et al., A new generation of dual-mode optical thermometry based on ZrO_2: Eu^{3+} nanocrystals. Nanophotonics **8**(12), 2347–2358 (2018). https://doi.org/10.1515/nanoph-2019-0359
50. J.M. Kim, S.M. Chang, S. Kim, K.-S. Kim, J. Kim et al., Design of SiO_2/ZrO_2 core–shell particles using the sol–gel process. Ceram. Int. **35**(3), 1243–1247 (2009). https://doi.org/10.1016/j.ceramint.2008.06.003
51. S. Kongwudthiti, P. Praserthdam, W. Tanakulrungsank, M. Inoue, The influence of Si–O–Zr bonds on the crystal-growth inhibition of zirconia prepared by the glycothermal method. J. Mater. Process. Technol. **136**(1–3), 186–189 (2003). https://doi.org/10.1016/S0924-0136(03)00157-2
52. J. Kaszewski, B.S. Witkowski, Wachnicki, T. Płociński, L.-I. Bulyk et al., Role of Zr^{3+} in excitation of Eu^{3+} ions in stabilized ZrO_2: Eu nanoparticles. J. Lumin. **273**, 120654 (2024). https://doi.org/10.1016/j.jlumin.2024.120654

53. H.S. Lokesha, M.L. Chithambo, A combined study of the thermoluminescence and electron paramagnetic resonance of point defects in ZrO_2: Er^{3+}. Radiat. Phys. Chem. **172**, 108767 (2020). https://doi.org/10.1016/j.radphyschem.2020.108767
54. J. Zhang, Y. Gao, X. Jia, J. Wang, Z. Chen et al., Oxygen vacancy-rich mesoporous ZrO_2 with remarkably enhanced visible-light photocatalytic performance. Sol. Energy Mater. Sol. Cells **182**, 113–120 (2018). https://doi.org/10.1016/j.solmat.2018.03.023
55. J.-M. Costantini, F. Beuneu, W.J. Weber, Radiation damage in cubic-stabilized zirconia. J. Nucl. Mater. **440**(1–3), 508–514 (2013). https://doi.org/10.1016/j.jnucmat.2013.02.041